UCLA
UCLA Previously Published Works

Title
Narrower Nanoribbon Biosensors Fabricated by Chemical Lift-off Lithography Show Higher Sensitivity

Permalink
https://escholarship.org/uc/item/7tf5t563

Journal
ACS Nano, 15(1)

ISSN
1936-0851

Authors
Zhao, Chuanzhen
Liu, Qingzhou
Cheung, Kevin M
et al.

Publication Date
2021-01-26

DOI
10.1021/acsnano.0c07503

Peer reviewed

eScholarship.org Powered by the California Digital Library
University of California

Author Manuscript

Author Manuscript

Author Manuscript

Author Manuscript

HHS Public Access

Author manuscript

ACS Nano. Author manuscript; available in PMC 2022 January 26.

Published in final edited form as:

ACS Nano. 2021 January 26; 15(1): 904–915. doi:10.1021/acsnano.0c07503.

Narrower Nanoribbon Biosensors Fabricated by Chemical Lift-Off Lithography Show Higher Sensitivity

Chuanzhen Zhao[†,§], **Qingzhou Liu**[□], **Kevin M. Cheung**[†,§], **Wenfei Liu**[†,§], **Qing Yang**[†,§], **Xiaobin Xu**[†,§], **Tianxing Man**[¶], **Paul S. Weiss**[†,§,▲,▼,*], **Chongwu Zhou**[□,#,*], **Anne M. Andrews**[†,§,▽,*]

[†]Department of Chemistry and Biochemistry, University of California, Los Angeles, Los Angeles, California 90095, United States

[§]California NanoSystems Institute, University of California, Los Angeles, Los Angeles, California 90095, United States

[□]Mork Family Department of Chemical Engineering and Materials Science, University of Southern California, Los Angeles, California 90089, United States

[¶]Department of Mechanical and Aerospace Engineering, University of California, Los Angeles, Los Angeles, California 90095, United States

[▲]Department of Bioengineering, University of California, Los Angeles, Los Angeles, California 90095, United States

[▼]Department of Materials Science and Engineering, University of California, Los Angeles, Los Angeles, California 90095, United States

[#]Ming Hsieh Department of Electrical Engineering, University of Southern California, Los Angeles, California 90089, United States

[▽]Department of Psychiatry and Biobehavioral Sciences, Semel Institute for Neuroscience and Human Behavior, and Hatos Center for Neuropharmacology, University of California, Los Angeles, Los Angeles, California 90095, United States

Abstract

[*]Corresponding Authors aandrews@mednet.ucla.edu (AMA), chongwuz@usc.edu (CZ), and psw@cnsi.ucla.edu (PSW).

Author Contributions

The experiments were designed by C. Zhao, QL, KMC, PSW, C. Zhou, and AMA. Data were collected by C. Zhao, QL, KMC, WL, QY, and XX, and analyzed by C. Zhao, QL, and AMA. The simulations were designed and performed by TM and CZ. Figures were prepared by C. Zhao and QL. The manuscript was written by C. Zhao, QL, KMC, PSW, C. Zhou, and AMA with assistance from all authors.

ASSOCIATED CONTENT

Supporting Information. The Supporting Information is available free of charge on the ACS Publication website at DOI:

Supplemental methods, Table S1, Table S2, Table S3, Figure S1, Figure S2, Figure S3, Figure S4, Figure S5, Figure S6, Figure S7, Figure S8: Elementally quantified EDX analysis; surface-to-volume ratios; statistics summary; EDX spectrum; optical microscope image of interdigitated electrodes; optical microscope images of 20-μm-wide In_2O_3 nanoribbons with source and drain electrodes; solid-state transfer characteristics of In_2O_3 FETs with different ribbon widths; gate leakage current in the liquid state; simulation results; liquid-state transfer characteristics of In_2O_3 FETs with different ribbon widths; schematic of FET for surface-to-volume ratio calculations, respectively.

Author Manuscript Author Manuscript Author Manuscript Author Manuscript

Wafer-scale nanoribbon field-effect transistor (FET) biosensors fabricated by straightforward top-down processes are demonstrated as sensing platforms with high sensitivity to a broad range of biological targets. Nanoribbons with 350-nm widths (700-nm pitch) were patterned by chemical lift-off lithography using high throughput, low-cost commercial digital versatile disks (DVDs) as masters. Lift-off lithography was also used to pattern ribbons with 2-μm or 20-μm widths (4-μm or 40-μm pitches, respectively) using masters fabricated by photolithography. For all widths, highly aligned, quasi-one-dimensional (1D) ribbon arrays were produced over centimeter length scales by sputtering to deposit 20-nm-thin-film In_2O_3 as the semiconductor. Compared to 20-μm-wide microribbons, FET sensors with 350-nm wide nanoribbons showed higher sensitivity to pH over a broad range (pH 5 to 10). Nanoribbon FETs functionalized with a serotonin-specific aptamer demonstrated larger responses to equimolar serotonin in high ionic strength buffer compared to microribbon FETs. Field-effect transistors with 350-nm-wide nanoribbons functionalized with single-stranded DNA showed greater sensitivity to detecting complementary DNA hybridization *vs* 20-μm microribbon FETs. In all, we illustrate facile fabrication and use of large-area, uniform In_2O_3 nanoribbon FETs for ion, small molecule, and oligonucleotide detection where higher surface-to-volume ratios translate to better detection sensitivities.

Graphical Abstract

Table of Contents Graphic and Synopsis

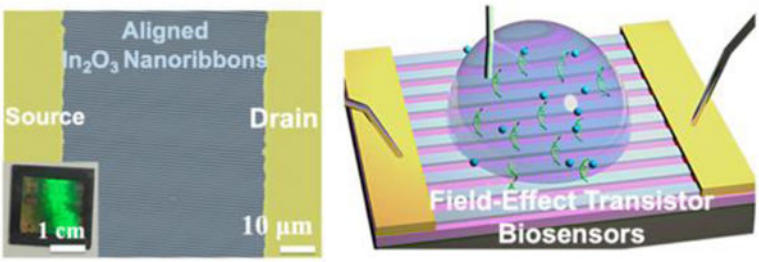

Keywords

chemical lift-off lithography; soft lithography; nanofabrication; small molecule sensing; DNA hybridization

Label-free, ultra-sensitive chemical and biological sensors that monitor biomarkers in body fluids and tissues have broad applications in healthcare and biomedical research, including cancer diagnostics,[1,2] DNA detection,[3–6] bacteria and virus detection,[7–9] and metabolite monitoring.[10–14] Developing sensors that provide accurate, real-time information regarding multiple analytes with high sensitivity and selectivity is at the heart of next-generation personalized medical devices, *e.g.*, point-of-care measurements, and implantable and wearable sensors.[15–25] Nanoelectronic field-effect transistor (FET) biosensors have been explored as platforms having unique properties and advantages towards the realization of these applications.

Indium oxide has been used to fabricate FET sensors with higher sensitivities, more straightforward surface functionalization, and greater stability in aqueous environments

Author Manuscript Author Manuscript Author Manuscript Author Manuscript

compared to other channel materials, including graphene and MoS_2.[26–28] Moreover, compared to other metal oxides, such as indium-gallium-zinc oxide, In_2O_3 is stable in buffers simulating physiological environments.[29,30] Bottom-up strategies were used to prepare In_2O_3 nanowires for use as gas sensors, chemical sensors, biosensors, and optical detectors.[31–34] However, similar to other bottom-up fabricated FETs, *e.g.,* Si nanowires or carbon nanotubes, bottom-up fabricated In_2O_3 nanowire sensors suffer from poor device-to-device reproducibility due to random orientations and variable numbers of nanowires between electrodes.[35,36]

In contrast, top-down fabrication strategies, *e.g.,* soft lithography, soft lithographic molecular printing,[37–39] nanoimprint lithography,[40,41] and nanotransfer printing[42–45] provide precise control over the morphologies and shapes of nanomaterials. Top-down In_2O_3 nanoribbons fabricated by straightforward photolithographic processes and low-temperature sputtering methods show high device uniformity and reproducibility.[30] We previously developed a lithography-free process involving sputtering In_2O_3 through shadow masks to fabricate ribbons of 25-μm width, ~16-nm thickness, and 500-μm length over cm scales.[30,46,47] These devices (previously referred to as nanoribbons due to the nanoscale height of the sputtered In_2O_3) had high field-effect mobilities (>13 $cm^2\ V^{-1}\ s^{-1}$), large current on/off ratios (>10^7),[30,46] and functioned as sensors in a variety of applications including pH sensing, cardiac biomarker detection, and wearable sensors for glucose monitoring.[30,46,47] Flexible multifunctional sensor arrays incorporating these 25-μm wide ribbons have also been developed to measure temperature, pH, and the neurotransmitters serotonin and dopamine, simultaneously.[48] Nonetheless, ribbons fabricated *via* shadow masks are limited in lateral resolution to tens of microns.

Surface-to-volume ratio is a critical parameter impacting nanobiosensor sensitivity, where higher ratios result in greater target sensitivities.[32,36,49–55] Here, we advance a generalizable, facile, top-down strategy for fabricating highly aligned In_2O_3 nanoribbons.[56,57] We employ chemical lift-off lithography (CLL), which is a soft lithography patterning approach that is cleanroom-free, high throughput, and high-fidelity, and enables micro- and nano-patterning to produce features as small as 15 nm.[58–65] In CLL, polydimethylsiloxane (PDMS) stamps with desired patterns are used to remove molecules self-assembled on Au surfaces selectively in the stamp contact areas. The remaining molecules in the noncontacted regions act as resists during wet etching to form three-dimensional features. We have used CLL to pattern Au micro- and nanostructures, including Au nanoribbon, disk, square, and circle arrays, and to pattern other metal and semiconductor surfaces.[26,56,62,66]

Here, we combined sputtering with CLL to produce 20-nm thin-film In_2O_3 ribbons at 350-nm, 2-μM, or 20-μM widths and wafer scales. As-fabricated ribbons were aligned between source and drain electrodes with controllable orientations, numbers, and sizes. Micro- and nanoribbon FET biosensors with different aspect ratios were characterized and compared. The 350-nm wide nanoribbon FETs showed greater sensitivities for target detection compared to 20-μm wide microribbon FETs providing further evidence for the concept that higher surface-to-volume ratios confer greater sensitivities in nanobiosensing applications.

Author Manuscript Author Manuscript Author Manuscript Author Manuscript

RESULTS AND DISCUSSION

The general In_2O_3 micro- and nanoribbon fabrication process is shown in Figure 1 and described in detail in Methods. We fabricated ribbon features for subsequent In_2O_3 sputtering followed by a process to remove Au/Ti features leaving behind In_2O_3 micro- or nanoribbons. We used commercial digital versatile disks-recordable (DVD-R) as templates to fabricate 350-nm-wide nanoribbons. These disks are economical, easily accessible masters (<$0.5/disc). Blank DVD-R disks contain sub-μm grating features.[56,57] The DVD-R masters were prepared by a straightforward separation and rinsing process as previously described.[54,55] Hard PDMS (*h*-PDMS) was used to replicate the high-aspect ratio DVD-R features.[56,57]

The DVD-R nanoribbon features, transfer of these features to *h*-PDMS, and further transfer to alkanethiol monolayers on Au has been characterized.[56,57] Previously, we deposited In_2O_3 *via* a sol-gel process with the Au/Ti layers deposited on top.[56] The SAMs on Au were then patterned. The Au/Ti areas that were not contacted by activated *h*-PDMS served as wet etching masks. The stamp-contacted/exposed Au/Ti features were etched to expose the underlying In_2O_3.

Our previous patterning approach resulted in overetching, which limited precise patterning.[56] Even when overetching was avoided, etching undercut the protective Au/Ti features to produce In_2O_3 nanoribbons that were narrower and less reproducible compared to the features of the masters.[56,57] Further, nanoribbons patterned using the previous method had a high degree of line-edge roughness. Here, we addressed these previous shortcomings by sputtering thin-film In_2O_3 *after* Au/Ti etching, resulting in high-fidelity In_2O_3 nanoribbons fabricated over large areas.

Sputtering of In_2O_3 was carried out normal to the substrate surface such that undercut of the Au/Ti structures did not influence the widths of the resulting In_2O_3 nanoribbons. Nanoribbons (350-nm) were imaged before and after the lift-off process using atomic force microscopy (AFM), as shown in Figure 2. Using the present fabrication process, In_2O_3 nanoribbons had heights of ~60 nm after In_2O_3 sputtering (Figure 2a), corresponding to the sum of the heights of the underlying Au and Ti layers. Sputtered does not add to the apparent height difference as In_2O_3 was sputtered atop both the patterned Au and the interleaved Si areas.

After removing the Au/Ti nanoribbon structures (and the overlying In_2O_3), uniform and continuous In_2O_3 nanoribbons with 350-nm widths and 20-nm heights remained, as shown *via* AFM (Figure 2b). To compare the widths and heights of the ribbons before and after removal of the Au templates, height profiles along the nanoribbons were analyzed (Figure 2c). The widths of In_2O_3 nanoribbons matched with the spacing between the Au nanoribbons demonstrating high-fidelity patterning and features characterized by sharp edges and high continuity.

Nanoribbons were fabricated on 1.5 cm × 1.5 cm Si wafers. The light blue In_2O_3 nanoribbon patterned region in the center of a representative wafer showed a strong iridescence when viewed at non-perpendicular angles under white light indicative of periodic (diffraction)

Author Manuscript Author Manuscript Author Manuscript Author Manuscript

grating patterns on the surface (Figure 2d). Scanning electron microscopy (SEM) indicated that nanoribbons were continuous over tens of microns and highly defined at the single nanoribbon scale (Figure 2e,f). Energy-dispersive X-ray (EDX) mapping was performed (Figure 2g), where the indium $L_{\alpha 1}$ energy of 3.286 keV (Figure S1) was mapped and calculated (Table S1). The EDX images showed In_2O_3 nanoribbons of ~350 nm widths, consistent with the results from AFM and SEM imaging.

To construct micro- and nanoribbon FETs, the orientations of well-aligned In_2O_3 structures were identified by AFM or SEM. Source and drain electrodes were then fabricated perpendicular to the nanoribbons (Figure 3a) or microribbons. The Au/Ti source and drain electrodes were deposited on top of as-prepared In_2O_3 ribbons *via* electron-beam (e-beam) evaporation. Interdigitated electrodes with lengths of 1300 μm and widths of 45 μm were prepared (Figure S2). Electrodes aligned well with as-fabricated 350-nm wide In_2O_3 nanoribbons, as shown in the SEM images in Figure 3b and 3c. Substrates with 2-μm or 20-μm wide In_2O_3 microribbons similarly demonstrated well-aligned configurations between the ribbons and electrodes (Figure 3d,3e, and Figure S3).

As discussed above and previously reported,[35,36] the orientations and numbers of nanowires or nanoribbons are challenging to control using bottom-up approaches. By contrast, using a top-down CLL patterning approach, orientations and numbers of ribbons were straightforwardly controllable based on the widths and pitches of the ribbons and the widths of the electrodes. For example, ~1850 350-nm wide In_2O_3 nanoribbons were incorporated and aligned with each pair of electrodes. Transistor performances were tested using a bottom-gate top-contact configuration, where p^{++} Si served as the bottom gate and SiO_2 as the gate dielectric (Figure 3f). Transfer and output curves for 350-nm wide In_2O_3 nanoribbon FETs are shown in Figure 3g and 3h, respectively, demonstrating current on/off ratios $>10^6$. The FETs with 2-μm or 20-μm wide ribbons, or continuous thin-film In_2O_3 FETs showed similar characteristics in solid state measurements (Figure S4).

The electrical performance of 350-nm-wide nanoribbon FET devices in a liquid environment was tested using solution gating, which corresponds to how devices were used for biosensing (*vide infra*). Each device was covered with a PDMS well filled with an electrolyte solution (Figure 4a). A Ag/AgCl reference electrode was used to apply a bias voltage through the electrolyte solution to gate each FET. Transfer and output curves for liquid-gated 350-nm wide In_2O_3 nanoribbon FETs in phosphate-buffered saline (PBS) are shown in Figure 4b and 4c, respectively. The nanoribbon FETs fabricated here operated in a liquid environment with current on/off ratios of 10^3, transfer curve saturation behavior, low gate leakage currents (Figure 4d, Figure S5), and low driving voltages. Microribbon FETs with different widths or continuous thin-film FETs showed similar liquid-state performance characteristics (Figure S6).

Ion-sensitive FETs (ISFETs), where FETs respond to changes in environmental ion concentrations, are used for a majority of FET chemical and biological sensing applications.[67–71] To investigate the performance of In_2O_3 nanoribbon ISFETs, we conducted pH sensing by systematically increasing the hydrogen ion concentrations of the solutions contacting FETs. We previously compared the pH sensitivities of 25-μm-wide In_2O_3 ribbon FET

Author Manuscript Author Manuscript Author Manuscript Author Manuscript

sensors having different ribbon heights.[30] Microribbons having thinner 10- or 20-nm In_2O_3 films showed higher sensitivities to pH compared to thicker microribbons, *e.g.*, 50-nm In_2O_3 films. Here, micro- and nanoribbons with constant 20-nm heights were used to compare the effects of changing ribbon widths.

Threshold voltage changes of ISFETs were determined for 350-nm-wide nanoribbons from pH 5 to 10. Representative transfer curves (drain current to gate voltage) are shown in Figure 4d. Time-related increases in drain current were observed with decreasing pH values (Figure 4e), which is typical for *n*-type semiconductor gate-voltage modulation behavior.[27,46,47] At lower pH values, there are greater numbers of positively charged hydrogen ions in solution leading to higher currents as more negative charge carriers are generated in *n*-type channels. Here, In_2O_3 was functionalized with (3-aminopropyl)triethoxysilane (APTES), where the terminal amine undergoes protonation and deprotonation with changes in pH. Notably, In_2O_3 FETs are less stable at low pH due to the chemical nature of metal oxides, which react with acids to form salts.[56]

Relative pH sensing responses for 350-nm- *vs* 20-μm-wide In_2O_3 nanoribbon FETs were compared (Figure 4f). Device currents for both configurations increased as the $[H^+]$ increased (*i.e.*, pH decreased). Surface-to-volume ratios for FETs with different ribbon widths were calculated (see Supporting Information, Figure S7). Ribbons with 350-nm widths had a 10% increase in surface-to-volume ratio compared to ribbons with 20-μm widths (Table S2). Yet, this modest increase in surface-to-volume ratio was sufficient to produce increased pH sensitivity, particularly at lower pH ($P<0.01$) (see Table S3 for full statistics). These findings provide evidence that FETs with nanoscale features having higher surface-to-volumes are associated with higher ion sensitivities.

Debye screening in high ionic strength solutions presents challenges for FET biosensing in physiological environments.[49,72,73] Overcoming Debye-length limitations enables the detection of biological targets *ex vivo* and *in vivo* to extend potential uses of FET biosensors for medical and biological applications, *e.g.*, sensing in body fluids for point-of-care or at-home monitoring. We developed aptamer-based FET biosensors for small-molecule detection under high ionic-strength conditions.[14,20,26] Aptamers, which are single-stranded oligonucleotides isolated specifically for adaptive target recognition, are functionalized on semiconductor surfaces. Upon target binding, aptamers undergo conformational rearrangements involving their negatively charged backbones (and associated solution ions) resulting in charge redistribution near semiconductor surfaces. Signal transduction arising from aptamer charge redistribution has enabled direct detection of charged, as well as neutral small-molecule targets under physiological conditions.[14]

Aptamers that selectively recognize serotonin were covalently immobilized on In_2O_3 (and SiO_2) ribbons (Figure 5a). Aptamers on the SiO_2 dielectric contribute minimally to target-induced currents. We conducted neurotransmitter sensing by adding increasing concentrations of serotonin into the PBS solutions above FETs. Representative transfer curves for 350-nm-wide In_2O_3 nanoribbon FETs at different serotonin concentrations are shown in Figure 5b. Calibrated response curves comparing the performance of 350-nm- *vs* 20-μm-wide ribbons both having 20-nm thin-film In_2O_3 are shown in Figure 5c.

Author Manuscript Author Manuscript Author Manuscript Author Manuscript

Nanoribbons with 350-nm widths showed a trend toward larger calibrated responses to serotonin compared to 20-μm-wide nanoribbons ($0.1<P<0.05$). Differences in performance for the two FET configurations were apparent at serotonin concentrations between 100 fM and 1 nM, where sensor responses were linear for both configurations but left-shifted for 350-nm-wide nanoribbons. Tuning nanoribbon widths provides another strategy for shifting overall device sensitivities, in addition to truncating or destabilizing aptamer stems and/or changing aptamer surface densities.[14,20] These strategies will be important for translation to *in vivo* sensing applications where target concentrations vary widely, *e.g.*, serotonin concentrations in the gut (micromolar range)[74] *vs* the brain extracellular space (nanomolar range).[75]

Previously, we found that even small changes in pH affect aptamer-FET sensor responses.[48] This effect was attributed to H^+-associated changes in charge redistribution around aptamers and near FET surfaces. For *in vivo* applications where the environmental pH varies, for example in conjunction with neuronal burst firing, we showed that incorporation of a separate pH sensor as part of a multiplexed device differentiated changes in pH from changes in neurotransmitter concentrations.[48] In prior work, we also carried out control experiments to determine target-specific detection using unfunctionalized FETs and FETs functionalized with a scrambled serotonin aptamer sequence, as well sensing in the presence of structurally similar interferants, which indicated that serotonin-aptamer FETs are highly selective.[14,48] Moreover, we have investigated real-time serotonin sensing (fM-μM) with a temporal resolution of ≤5 s, which was limited by the measurement system response time.[48]

In addition to ions and small molecules, oligonucleotide sensing is important for clinical diagnostics, such as genotyping for cancer immunotherapy and for diagnosing infectious diseases.[5,6,76–79] Here, label-free DNA detection was performed on micro- and nanoribbon FET biosensors. Thiolated single-stranded DNA (ssDNA) was covalently immobilized onto In_2O_3 (and SiO_2). Solutions containing 10^6 to 10^{15} copies of complementary oligonucleotide (~1 fM to ~1 μM) were added to the sensing environment in artificial cerebrospinal fluid (aCSF) (Figure 5d). The aCSF was diluted 10-fold to increase the Debye length and thereby, to maximize low copy-number detection.

Representative transfer curves for 350-nm-wide In_2O_3 nanoribbon FETs at different target DNA copy numbers are shown in Figure 5e. Calibrated responses are compared in Figure 5f for the performance of 350-nm-nanoribbon *vs* 20-μm-microribbon In_2O_3 FETs. Nanoribbons with 350-nm widths showed higher sensitivity to DNA hybridization than 20-μm-wide microribbons ($P<0.05$).

The direction of change for *n*-type In_2O_3 FET transfer characteristics is due to gating effects associated with negatively charged oligonucleotides.[14,20] For aptamer-based sensing, the serotonin aptamers used here reorient away from FET surfaces upon target binding resulting in increases in concentration-related currents in *i*-V sweeps due to increased transconductance.[14] For DNA hybridization, decreases in currents in the *i*-V sweeps with increasing DNA concentrations are due to the accumulation of net negative surface charge, which occurs upon DNA hybridization.[76] In a previous study, we observed negligible sensor responses to noncomplementary target sequences.[76] We differentiated sequences with

Author Manuscript Author Manuscript Author Manuscript Author Manuscript

single-base mismatches. The highly sensitive platform developed here and in our recent work[76] portends a reagentless strategy for oligonucleotide (DNA, RNA) sensing, which can be developed for the detection of a wide variety of infectious agents, including the severe acute respiratory-related coronavirus 2 (SARS-CoV-2).[79,80]

Relationships between FET sensitivity and surface-to-volume ratio have been investigated using different types of channel materials.[32,36,49–55] Silicon nanowires with dimensions ≥50 nm have been most often investigated.[36,50,54] Silicon nanowires with higher surface-to-volume ratios have higher sensitivities towards pH, protein, and DNA detection.[36,50,54] For example, Linnros and colleagues studied silicon-on-insulator (SOI) nanowires with widths of 50–170 nm fabricated by electron-beam lithography having a 100-nm semiconductor layer.[54] For their smallest, 50-nm, nanowires, the surface-to-volume ratio was only 2/100 nm^{-1} (*i.e.*, 0.4/20 nm^{-1}), which is 60% less than the surface-to-volume ratio of our 20-nm-thin-film In_2O_3 FETs (*i.e.*, 1/20 nm^{-1}; see Supporting Information for calculations and Table S2).

For bottom-up fabricated cylindrical nanowires, the surface-volume-ratio is related to 2/r, where r is the nanowire radius. In principle, Si nanowires with diameters larger than 80 nm (*i.e.*, surface-to-volume ratio 1/20 nm^{-1}) have surface-to-volume ratios lower than the microribbon, nanoribbon, and thin-film FETs investigated here. For instance, Sun and coworkers produced Si nanowire devices for sensing protein adsorption.[36] Fabrication involved nanowire contract printing and SEM to select and to remove nanowires individually producing devices with specific numbers and diameters of nanowire. Single nanowire devices were grouped by diameter ranges (*i.e.*, 60–80 nm, 81–100 nm, and 101–120 nm). The smallest 60-nm nanowires had surface-to-volume ratios of 2/30 nm^{-1} (*i.e.*, 1.3/20 nm^{-1}) —a 17% increase over the surface-to-volume ratio of the 350-nm nanoribbons investigated here (Table S2).

Williams and co-authors explored the effects of surface-to-volume ratio in the context of ssDNA hybridization with complementary single-stranded peptide nucleic acids functionalized on Si nanowire FETs having widths of 50, 100, 200, 400, and 800 nm.[50] The Si semiconductor layer was 50 nm. For these sensors, the signal-to-volume ratios were 3/50, 2/50, 1.5/50, 1.25/50, and 1.125/50, respectively (*i.e.*, 1.2/20, 0.8/20. 0.6/20, 0.5/20, and 0.45/20, respectively). Hybridization sensitivity was linear for nanowires with widths between 800 and 100 nm. A sharp increase in sensitivity to DNA hybridization for the 50-nm-wide Si nanowires was attributed to nonlinear increases in conductance at small nanowire diameters, which was determined experimentally and *via* simulation.

For In_2O_3 nanoribbon FETs, sensor sensitivity can be increased by reducing nanoribbon dimensions using In_2O_3 sol-gel processing to produce thinner semiconductor layers[26,27,56] and/or *via* CLL with masters fabricated by e-beam lithography to pattern features as small as 15 nm.[58–65] To extend our findings beyond the two feature sizes investigated experimentally, we performed finite element analysis simulations to predict FET sensitivities with respect to a number of different nanoribbon widths. As shown in Figure S8, increased sensitivity was predicted for FETs with smaller widths given the same In_2O_3 thickness (20 nm), which is attributed to higher surface-to-volume ratios. Similar to the findings of Williams and

Author Manuscript Author Manuscript Author Manuscript Author Manuscript

colleagues, we observed the greatest increases in FET responses for features with widths <100 nm.[50]

Here, we focused on top-down approaches using soft lithography. Traditional top-down approaches, such as e-beam lithography (EBL), also offer precise control over the orientations, sizes, and numbers of quasi-1D nanostructures, thereby enabling fabrication of biosensors with high reproducibility.[81] Nonetheless, top-down fabrication of sub-micron features needed to achieve high surface-to-volume ratios requires techniques that are challenging to translate for broad applications. For example, commonly used EBL methods are low throughput and suffer from high equipment and usage costs.

Bottom-up approaches involving 1D nanomaterials, *e.g.*, Si nanowires (SiNWs), have also been used to fabricate FETs with high surface-to-volume ratios, which increased device sensitivities.[82–84] However, fabrication of Si-based nanomaterials, including SiNWs, often relies on silicon-on-insulator wafers, which are considerably more expensive (>$500 per 4” wafer) than standard Si wafers (<$50 per 4” wafer).[85] Together, these drawbacks present significant barriers to the use of many types of nanomaterials in actual biomedical applications, and necessitate the development of high throughput, cost-effective, and precise fabrication strategies for biosensors, such as the method described herein.

CONCLUSIONS AND PROSPECTS

Highly aligned In_2O_3 nanoribbon FETs were fabricated by chemical lift-off lithography using commercially available DVD-R disks as nanostructured templates and low-temperature sputtering to produce 20-nm In_2O_3 thin-films. Nanoribbon FET sensors have high surface-to-volume ratios that imparted greater sensitivity for ion, small-molecule, and oligonucleotide detection, all other factors being equal. The fabrication and sensing approaches reported herein represent generalizable strategies for improving electronic biosensing by fabricating high surface-to-volume ratio nanoscale features for applications where high and/or tunable sensitivities are critical.

This top-down, large-scale nanolithography strategy to fabricate metal-oxide nanoribbons can be implemented as a high-throughput, cost-effective, cleanroom-free means of production. Even so, nanostructure surface-to-volume ratio is only one of many parameters that impacts nanobiosensor sensitivity. Other factors include semiconductor material, doping, and nanowire/nanostructure densities. If surface receptors are employed for selective biosensing, receptor type (*e.g.*, protein, nucleic acid), density, and target affinity, as well as the ionic strength of the sensing environment and biofouling will influence performance. Nonetheless, we demonstrate unequivocally through experimentation and simulation that surface-to-volume ratio impacts biosensor responses under physiologically relevant conditions.

Author Manuscript Author Manuscript Author Manuscript Author Manuscript

MATERIALS AND METHODS

Materials.

Prime quality 4″ Si wafers (P/B, 0.001–0.005 Ω-cm, thickness 500 μm) were purchased from Silicon Valley Microelectronics, Inc. (Santa Clara, CA). Sylgard 184® silicone elastomer kits (lot #0008823745) were purchased from Ellsworth Adhesives (Germantown, WI). Indium(III) nitrate hydrate (99.999%), iron nitrate, thiourea, ammonium hydroxide (30% w/v in H_2O), hydrogen peroxide (30% v/v in H_2O), ethylenediaminetetraacetic acid disodium salt dihydrate (EDTA), 3-phosphonopropioninc acid, (3-aminopropyl)triethoxysilane (APTES), trimethoxy(propyl)silane, and 3-maleimidobenzoic acid *N*-hydroxysuccinimide (MBS) were purchased from Sigma-Aldrich (St. Louis, MO) and used as received. UltraPure™ nuclease-free distilled water was purchased from Thermo Fisher Scientific (Waltham, MA) and used as received. The masters templated for lift-off lithography were commercially available DVD-R recordable 16× speed 4.7 GB blank discs (Memorex).

Water was deionized before use (18.2 MΩ-cm) using a Milli-Q system (Millipore, Billerica, MA). The serotonin aptamer (/5ThioMC6-D/CG ACT GGT AGG CAG ATA GGG GAA GCT GAT TCG ATG CGT GGG TCG), thiolated ssDNA (/5ThioMC6-D/GG TTC TTG GAT ATA G), and complementary ssDNA (CTA TAT CCA AGA ACC) were synthesized by Integrated DNA Technologies, Inc. (Coralville, IA). The Ag/AgCl reference electrodes were purchased from World Precision Instruments, Inc. (Sarasota, FL).

Buffer solutions.

Phosphate-buffered saline solution was purchased from Thermo Fisher Scientific (Waltham, MA, #10010023) and used as received. Artificial cerebrospinal fluid solution was NaCl (14.7 mM), KCl (0.35 mM), $CaCl_2$ (0.1 mM), NaH_2PO_4 (0.1 mM), $NaHCO_3$ (0.25 mM), and $MgCl_2$ (0.12 mM). A detailed procedure for preparation appears in Supplemental Information.

Fabrication of masters.

Photomasks for 2-μm-wide and 4-μm-pitch lines or 20-μm-wide and 40-μm-pitch lines were designed using the AutoCAD software suite (Autodesk, Inc.). Positive photoresist SPR700–1.2 (Rohm & Haas Co., Philadelphia, PA) was used for patterning Si by photolithography. The exposed Si was selectively etched using deep reactive ion etching (Plasma-Therm, LLC, Petersburg, FL). The resulting masters were then coated with trichloro(1H,1H,2H,2H-perfluorooctyl) silane as a release layer. The DVD-R masters for 350-nm-wide nanoribbons were prepared by a separation and rinsing process as previously described.[56,57]

Fabrication of In_2O_3 micro- and nanoribbon FETs.

The general fabrication process is illustrated in Figure 1. The Si substrates with 100 nm SiO_2 were coated with 30-nm Ti followed by 30-nm Au using a CHA solution electron-beam evaporator (CHA Industries, Inc., Fremont, CA) under high vacuum (10^{-8} Torr) at an evaporation rate of 0.1 nm/s. Preparation of *h*-PDMS stamps, CLL patterning, and wet etching processes for nanoribbon fabrication were carried out as previously reported.[56,57]

Author Manuscript Author Manuscript Author Manuscript Author Manuscript

Briefly, an ethanolic 1 mM solution of 11-mercapto-1-undecanol was used to form SAMs on Au surfaces by incubation with substrates for 12 h. Oxygen-plasma-activated DVD-templated *h*-PDMS stamps were brought into contact with SAMs. The soft PDMS stamps for CLL patterning of 2-μm and 20-μm ribbons were made from Si masters fabricated by conventional photolithography, as described above. The CLL was carried out similar to patterning for 350-nm nanoribbons.

For all formats, upon stamp removal, SAM molecules in the stamp-contacted areas were selectively removed, along with monolayers of Au atoms.[58,64] After the CLL process, Au etchant composed of 20 mM iron nitrate and 30 mM thiourea was used to etch the Au films (~30 min). A Ti etchant (113 mM EDTA, 3% hydrogen peroxide (v/v in H_2O), and 1.26% ammonia hydroxide solution (w/v in H_2O)) was used to etch to Ti for ~9 min. Wet etching transferred the patterns through the metal layers. After wet etching, substrates were oxygen-plasma treated to remove remaining SAM molecules in the non-contact areas prior to In_2O_3 sputtering.

The In_2O_3 (~20 nm) was deposited onto the patterned substrates using a radio frequency (RF) sputtering process (Denton Discovery 550 Sputtering System, Nanoelectronics Research Facility (NRF), University of California, Los Angeles (UCLA)). Sputtering is a room temperature process, which is compatible with a variety of substrates including Si, glass, polyesters, and polyimide.[30,46,47] Metal removal was then performed by immersing substrates into Ti etchant for ~9 min under ultrasonication (Branson Ultrasonics, Danbury, CT), leaving In_2O_3 micro- or nanoribbons on Si/SiO_2 substrates. Devices were cleaned with water and dried under N_2 before measurements or further functionalization. Source/drain electrodes of 10-nm thick Ti and 50-nm thick Au were defined by conventional photolithography and deposited using a solution electron-beam evaporator (CHA Industries, Inc., Fremont, CA) under high vacuum (10^{-8} Torr) with an evaporation rate of 0.1 nm/s. An optical microscope image of the electrode configuration with respect to In_2O_3 nanoribbons is shown in Figure S2.

Characterization.

Scanning electron microscope images were obtained using a Supra 40VP scanning electron microscope with an Inlens SE Detector (Carl Zeiss Microscopy, LLC, White Plains, NY). Atomic force microscope imaging was performed using a FastScan AFM with ScanAsyst-Air tips (Bruker, Billerica, MA). Electronic FET measurements were carried out on a manual analytical probe station (Signatone, Gilroy, CA) equipped with a Keithley 4200A SCS (Tektronix, Beaverton, OR) or an Agilent 4156B semiconductor parameter analyzer (Santa Clara, CA). Optical images were taken with a digital camera attached to a Zeiss Axiotech optical microscope.

Biosensing.

For pH sensing, In_2O_3 surfaces were functionalized with APTES. Real-time source-drain current measurements were performed (*i*-t), where the gate voltage (V_{GS}) was held at 300 mV and the drain voltage (V_D) was held at 100 mV throughout. Buffer solutions of pH 7.4

Author Manuscript Author Manuscript Author Manuscript Author Manuscript

were used to obtain stable baselines. Buffer solutions from pH 10 to 5 were sequentially added and removed using pipettes.

Thiolated serotonin aptamer or thiolated ssDNA (1 μM in nuclease-free water) were immobilized onto the oxide surfaces of FETs using APTES/PTMS (1:9, v/v) and MBS ester as linkers. Serotonin (final concentration 10 fM-1 μM) or complementary ssDNA (final concentration 1 fM-1 μM) in 1 μL aliquots were added into the buffer solutions (39 μL) over FETs and mixed with a pipette.

Source-drain current (I_{DS}) transfer curves were obtained, wherein gate voltages (V_{GS}) were applied from −200 to 400 mV with a step voltage of 5 mV, while the drain voltage (V_D) was held at 10 mV throughout. Five gate-voltage sweeps were repeated (five sweeps at 0, 5, and 10 min). The sweeps at each time point were averaged to determine each transfer curve. Calibrated responses were calculated by dividing the absolute sensor response (ΔI), which takes into account baseline subtraction, by the change in source-drain current with voltage sweep ($\Delta I_{DS}/\Delta V_G$).[14]

Statistics.

Data for pH, serotonin, and ssDNA sensing were analyzed by two-way analysis of variance with ribbon width and target concentration as the independent variables (GraphPad Prism 7.04, San Diego, CA). Data for 10 nM, 100 nM, and 1 μM serotonin were excluded from the statistical analysis because sensor responses were saturated (Fig. 5c). Two data points from the 20-μm-wide nanoribbon DNA sensing data were excluded from plotting and analysis due to external disturbance of the Ag/AgCl reference electrode noted during the measurements (Fig. 5f).

Simulations.

The COMSOL Multiphysics 5.2 program was used to simulate the relative responses of nanoribbons having different widths. Details for the model are from Shoorideh and Chui.[86] Here, In_2O_3 nanoribbons were designated to be 2 μm long and 20 nm thick, with widths varying from 5 nm to 20 μm. The In_2O_3 is intrinsically doped by oxygen vacancies at an estimated concentration of 2.5×10^{16} cm^{-3} *n*-type doping.[30] The substrate was 200-nm silicon dioxide. A surface charge density of 1.6×10^{-3} C/m^{-2} was added to model aptamer-induced charge change on the channels and the SiO_2 surface. Semiconductor physics was applied to compute the source-drain electric current when sweeping the gate voltage. The sensitivity was then calculated based on previous work.[14]

Supplementary Material

Refer to Web version on PubMed Central for supplementary material.

ACKNOWLEDGMENTS

This work was supported by the National Institute on Drug Abuse (DA045550) and the National Science Foundation (CMMI-1636136). We acknowledge the facilities and thank the staff of the Nanoelectronics Research Facility, Electron Imaging Center, Nano & Pico Characterization Lab, and Integrated Systems Nanofabrication Cleanroom of the California NanoSystems Institute, UCLA. KMC acknowledges support from an SG fellowship from the Department of Chemistry and Biochemistry at UCLA. C. Zhou and QL acknowledge support from King

Author Manuscript Author Manuscript Author Manuscript Author Manuscript

Abdul-Aziz City for Science and Technology (KACST). We thank Ms. Zhiyuan Zhao for technical assistance, Dr. John M. Abendroth for assistance with schematic designs, and Dr. Ken Sagynbekov and Ms. Merel Dagher for helpful discussions on statistical analysis.

REFERENCES

(1). Arya SK; Bhansali S. Lung Cancer and Its Early Detection Using Biomarker-Based Biosensors. Chem. Rev 2011, 111, 6783–6809. [PubMed: 21774490]

(2). Huang X; Liu Y; Yung B; Xiong Y; Chen X. Nanotechnology-Enhanced No-Wash Biosensors for in Vitro Diagnostics of Cancer. ACS Nano 2017, 11, 5238–5292. [PubMed: 28590117]

(3). Hahm J.-i.; Lieber CM Direct Ultrasensitive Electrical Detection of DNA and DNA Sequence Variations Using Nanowire Nanosensors. Nano Lett. 2004, 4, 51–54.

(4). Sorgenfrei S; Chiu CY; Gonzalez RL Jr.; Yu YJ; Kim P; Nuckolls C; Shepard KL Label-Free Single-Molecule Detection of DNA-Hybridization Kinetics with a Carbon Nanotube Field-Effect Transistor. Nat. Nanotechnol 2011, 6, 126–132. [PubMed: 21258331]

(5). Ping J; Vishnubhotla R; Vrudhula A; Johnson AT Scalable Production of High-Sensitivity, Label-Free DNA Biosensors Based on Back-Gated Graphene Field Effect Transistors. ACS Nano 2016, 10, 8700–8704. [PubMed: 27532480]

(6). Blair EO; Corrigan DK A Review of Microfabricated Electrochemical Biosensors for DNA Detection. Biosens. Bioelectron 2019, 134, 57–67. [PubMed: 30954927]

(7). Patolsky F; Zheng G; Hayden O; Lakadamyali M; Zhuang X; Lieber CM Electrical Detection of Single Viruses. Proc. Natl. Acad. Sci. U. S. A 2004, 101, 14017–14022. [PubMed: 15365183]

(8). Miranda OR; Li X; Garcia-Gonzalez L; Zhu ZJ; Yan B; Bunz UH; Rotello VM Colorimetric Bacteria Sensing Using a Supramolecular Enzyme-Nanoparticle Biosensor. J. Am. Chem. Soc 2011, 133, 9650–9653. [PubMed: 21627131]

(9). Seo G; Lee G; Kim MJ; Baek SH; Choi M; Ku KB; Lee CS; Jun S; Park D; Kim HG; Kim SJ; Lee JO; Kim BT; Park EC; Kim SI Rapid Detection of COVID-19 Causative Virus (SARS-CoV-2) in Human Nasopharyngeal Swab Specimens Using Field-Effect Transistor-Based Biosensor. ACS Nano 2020, 14, 5135–5142. [PubMed: 32293168]

(10). Gao W; Emaminejad S; Nyein HYY; Challa S; Chen K; Peck A; Fahad HM; Ota H; Shiraki H; Kiriya D; Lien DH; Brooks GA; Davis RW; Javey A. Fully Integrated Wearable Sensor Arrays for Multiplexed in Situ Perspiration Analysis. Nature 2016, 529, 509–514. [PubMed: 26819044]

(11). Koh A; Kang D; Xue Y; Lee S; Pielak RM; Kim J; Hwang T; Min S; Banks A; Bastien P; Manco MC; Wang L; Ammann KR; Jang KI; Won P; Han S; Ghaffari R; Paik U; Slepian MJ; Balooch G; et al. A Soft, Wearable Microfluidic Device for the Capture, Storage, and Colorimetric Sensing of Sweat. Sci. Transl. Med 2016, 8, 366ra165.

(12). Zhang Y; Clausmeyer J; Babakinejad B; Cordoba AL; Ali T; Shevchuk A; Takahashi Y; Novak P; Edwards C; Lab M; Gopal S; Chiappini C; Anand U; Magnani L; Coombes RC; Gorelik J; Matsue T; Schuhmann W; Klenerman D; Sviderskaya EV; et al. Spearhead Nanometric Field-Effect Transistor Sensors for Single-Cell Analysis. ACS Nano 2016, 10, 3214–3221. [PubMed: 26816294]

(13). Emaminejad S; Gao W; Wu E; Davies ZA; Yin Yin Nyein H; Challa S; Ryan SP; Fahad HM; Chen K; Shahpar Z; Talebi S; Milla C; Javey A; Davis RW Autonomous Sweat Extraction and Analysis Applied to Cystic Fibrosis and Glucose Monitoring Using a Fully Integrated Wearable Platform. Proc. Natl. Acad. Sci. U. S. A 2017, 114, 4625–4630. [PubMed: 28416667]

(14). Nakatsuka N; Yang KA; Abendroth JM; Cheung KM; Xu X; Yang H; Zhao C; Zhu B; Rim YS; Yang Y; Weiss PS; Stojanović MN; Andrews AM Aptamer-Field-Effect Transistors Overcome Debye Length Limitations for Small-Molecule Sensing. Science 2018, 362, 319–324. [PubMed: 30190311]

(15). Pollock NR; Rolland JP; Kumar S; Beattie PD; Jain S; Noubary F; Wong VL; Pohlmann RA; Ryan US; Whitesides GM A Paper-Based Multiplexed Transaminase Test for Low-Cost, Point-Of-Care Liver Function Testing. Sci. Transl. Med 2012, 4, 152ra129.

(16). Kim J; Lee M; Shim HJ; Ghaffari R; Cho HR; Son D; Jung YH; Soh M; Choi C; Jung S; Chu K; Jeon D; Lee ST; Kim JH; Choi SH; Hyeon T; Kim DH Stretchable Silicon Nanoribbon Electronics for Skin Prosthesis. Nat. Commun 2014, 5, 5747. [PubMed: 25490072]

Author Manuscript Author Manuscript Author Manuscript Author Manuscript

(17). Liu R; Chen R; Elthakeb AT; Lee SH; Hinckley S; Khraiche ML; Scott J; Pre D; Hwang Y; Tanaka A; Ro YG; Matsushita AK; Dai X; Soci C; Biesmans S; James A; Nogan J; Jungjohann KL; Pete DV; Webb DB; et al. High Density Individually Addressable Nanowire Arrays Record Intracellular Activity from Primary Rodent and Human Stem Cell Derived Neurons. Nano Lett. 2017, 17, 2757–2764. [PubMed: 28384403]

(18). Taylor IM; Du Z; Bigelow ET; Eles JR; Horner AR; Catt KA; Weber SG; Jamieson BG; Cui XT Aptamer-Functionalized Neural Recording Electrodes for the Direct Measurement of Cocaine in Vivo. J. Mater. Chem. B 2017, 5, 2445–2458. [PubMed: 28729901]

(19). Bariya M; Nyein HYY; Javey A. Wearable Sweat Sensors. Nat. Electron 2018, 1, 160–171.

(20). Cheung KM; Yang KA; Nakatsuka N; Zhao C; Ye M; Jung ME; Yang H; Weiss PS; Stojanović MN; Andrews AM Phenylalanine Monitoring via Aptamer-Field-Effect Transistor Sensors. ACS Sens. 2019, 4, 3308–3317. [PubMed: 31631652]

(21). Kim J; Campbell AS; de Avila BE; Wang J. Wearable Biosensors for Healthcare Monitoring. Nat. Biotechnol 2019, 37, 389–406. [PubMed: 30804534]

(22). Gao W; Ota H; Kiriya D; Takei K; Javey A. Flexible Electronics toward Wearable Sensing. Acc. Chem. Res 2019, 52, 523–533. [PubMed: 30767497]

(23). Wen X; Wang B; Huang S; Liu TL; Lee MS; Chung PS; Chow YT; Huang IW; Monbouquette HG; Maidment NT; Chiou PY Flexible, Multifunctional Neural Probe with Liquid Metal Enabled, Ultra-Large Tunable Stiffness for Deep-Brain Chemical Sensing and Agent Delivery. Biosens. Bioelectron 2019, 131, 37–45. [PubMed: 30818131]

(24). Scida K; Plaxco KW; Jamieson BG High Frequency, Real-Time Neurochemical and Neuropharmacological Measurements in Situ in the Living Body. Transl. Res 2019, 213, 50–66. [PubMed: 31361988]

(25). He X; Yang S; Pei Q; Song Y; Liu C; Xu T; Zhang X. Integrated Smart Janus Textile Bands for Self-Pumping Sweat Sampling and Analysis. ACS Sens. 2020, 5, 1548–1554. [PubMed: 32466645]

(26). Kim J; Rim YS; Chen H; Cao HH; Nakatsuka N; Hinton HL; Zhao C; Andrews AM; Yang Y; Weiss PS Fabrication of High-Performance Ultrathin In2O3 Film Field-Effect Transistors and Biosensors Using Chemical Lift-Off Lithography. ACS Nano 2015, 9, 4572–4582. [PubMed: 25798751]

(27). Rim YS; Bae SH; Chen H; Yang JL; Kim J; Andrews AM; Weiss PS; Yang Y; Tseng HR Printable Ultrathin Metal Oxide Semiconductor-Based Conformal Biosensors. ACS Nano 2015, 9, 12174–12181. [PubMed: 26498319]

(28). Chen H; Rim YS; Wang IC; Li C; Zhu B; Sun M; Goorsky MS; He X; Yang Y. Quasi-Two-Dimensional Metal Oxide Semiconductors Based Ultrasensitive Potentiometric Biosensors. ACS Nano 2017, 11, 4710–4718. [PubMed: 28430412]

(29). Jin SH; Kang SK; Cho IT; Han SY; Chung HU; Lee DJ; Shin J; Baek GW; Kim TI; Lee JH; Rogers JA Water-Soluble Thin Film Transistors and Circuits Based on Amorphous Indium-Gallium-Zinc Oxide. ACS Appl. Mater. Interfaces 2015, 7, 8268–8274. [PubMed: 25805699]

(30). Aroonyadet N; Wang X; Song Y; Chen H; Cote RJ; Thompson ME; Datar RH; Zhou C. Highly Scalable, Uniform, and Sensitive Biosensors Based on Top-Down Indium Oxide Nanoribbons and Electronic Enzyme-Linked Immunosorbent Assay. Nano Lett. 2015, 15, 1943–1951. [PubMed: 25636984]

(31). Li C; Zhang D; Liu X; Han S; Tang T; Han J; Zhou C. In_2O_3 Nanowires as Chemical Sensors. Appl. Phys. Lett 2003, 82, 1613–1615.

(32). Zhang D; Liu Z; Li C; Tang T; Liu X; Han S; Lei B; Zhou C. Detection of NO_2 Down to ppb Levels Using Individual and Multiple In_2O_3 Nanowire Devices. Nano Lett 2004, 4, 1919–1924.

(33). Tang T; Liu X; Li C; Lei B; Zhang D; Rouhanizadeh M; Hsiai T; Zhou C. Complementary Response of In_2O_3 Nanowires and Carbon Nanotubes to Low-Density Lipoprotein Chemical Gating. Appl. Phys. Lett 2005, 86, 103903.

(34). Curreli M; Li C; Sun Y; Lei B; Gundersen MA; Thompson ME; Zhou C. Selective Functionalization of In_2O_3 Nanowire Mat Devices for Biosensing Applications. J. Am. Chem. Soc 2005, 127, 6922–6923. [PubMed: 15884914]

Author Manuscript Author Manuscript Author Manuscript Author Manuscript

(35). Lee BY; Sung MG; Lee J; Baik KY; Kwon YK; Lee MS; Hong S. Universal Parameters for Carbon Nanotube Network-Based Sensors: Can Nanotube Sensors Be Reproducible? ACS Nano 2011, 5, 4373–4379. [PubMed: 21615164]

(36). Li J; Zhang Y; To S; You L; Sun Y. Effect of Nanowire Number, Diameter, and Doping Density on Nano-FET Biosensor Sensitivity. ACS Nano 2011, 5, 6661–6668. [PubMed: 21815637]

(37). Xia Y; Rogers JA; Paul KE; Whitesides GM Unconventional Methods for Fabricating and Patterning Nanostructures. Chem. Rev 1999, 99, 1823–1848. [PubMed: 11849012]

(38). Mizuno H; Buriak JM Catalytic Stamp Lithography for Sub-100 nm Patterning of Organic Monolayers. J. Am. Chem. Soc 2008, 130, 17656–17657. [PubMed: 19063631]

(39). Braunschweig AB; Huo F; Mirkin CA Molecular Printing. Nat. Chem 2009, 1, 353–358. [PubMed: 21378889]

(40). Wang H; Haroldson R; Balachandran B; Zakhidov A; Sohal S; Chan JY; Zakhidov A; Hu W. Nanoimprinted Perovskite Nanograting Photodetector with Improved Efficiency. ACS Nano 2016, 10, 10921–10928. [PubMed: 28024335]

(41). Wang C; Shao J; Lai D; Tian H; Li X. Suspended-Template Electric-Assisted Nanoimprinting for Hierarchical Micro-Nanostructures on a Fragile Substrate. ACS Nano 2019, 13, 10333–10342. [PubMed: 31437390]

(42). Meitl MA; Zhu Z-T; Kumar V; Lee KJ; Feng X; Huang YY; Adesida I; Nuzzo RG; Rogers JA Transfer Printing by Kinetic Control of Adhesion to an Elastomeric Stamp. Nat. Mater 2005, 5, 33–38.

(43). Seo MH; Yoo JY; Choi SY; Lee JS; Choi KW; Jeong CK; Lee KJ; Yoon JB Versatile Transfer of an Ultralong and Seamless Nanowire Array Crystallized at High Temperature for Use in High-Performance Flexible Devices. ACS Nano 2017, 11, 1520–1529. [PubMed: 28135071]

(44). Han HJ; Jeong JW; Yang SR; Kim C; Yoo HG; Yoon JB; Park JH; Lee KJ; Kim TS; Kim SW; Jung YS Nanotransplantation Printing of Crystallographic-Orientation-Controlled Single-Crystalline Nanowire Arrays on Diverse Surfaces. ACS Nano 2017, 11, 11642–11652. [PubMed: 29131582]

(45). Lee SH; Shin SH; Madsen M; Takei K; Nah J; Lee MH A Soft Lithographic Approach to Fabricate InAs Nanowire Field-Effect Transistors. Sci. Rep 2018, 8, 3204. [PubMed: 29453402]

(46). Liu Q; Aroonyadet N; Song Y; Wang X; Cao X; Liu Y; Cong S; Wu F; Thompson ME; Zhou C. Highly Sensitive and Quick Detection of Acute Myocardial Infarction Biomarkers Using In2O3 Nanoribbon Biosensors Fabricated Using Shadow Masks. ACS Nano 2016, 10, 10117–10125. [PubMed: 27934084]

(47). Liu Q; Liu Y; Wu F; Cao X; Li Z; Alharbi M; Abbas AN; Amer MR; Zhou C. Highly Sensitive and Wearable In2O3 Nanoribbon Transistor Biosensors with Integrated On-Chip Gate for Glucose Monitoring in Body Fluids. ACS Nano 2018, 12, 1170–1178. [PubMed: 29338249]

(48). Liu Q; Zhao C; Chen M; Liu Y; Zhao Z; Wu F; Li Z; Weiss PS; Andrews AM; Zhou C. Flexible Multifunctional In2O3 Nanoribbon Aptamer-Field-Effect Transistor Biosensing. iScience 2020, 23, 101469.

(49). Nair PR; Alam MA Screening-Limited Response of Nanobiosensors. Nano Lett. 2008, 8, 1281–1285. [PubMed: 18386914]

(50). Li Z; Rajendran B; Kamins TI; Li X; Chen Y; Williams RS Silicon Nanowires for Sequence-Specific DNA Sensing: Device Fabrication and Simulation. Appl. Phys. A 2005, 80, 1257–1263.

(51). Sheehan PE; Whitman LJ Detection Limits for Nanoscale Biosensors. Nano Lett. 2005, 5, 803–807. [PubMed: 15826132]

(52). Zhiyong F; Lu JG Chemical Sensing with ZnO Nanowire Field-Effect Transistor. IEEE Trans. Nanotechnol 2006, 5, 393–396.

(53). Stern E; Klemic JF; Routenberg DA; Wyrembak PN; Turner-Evans DB; Hamilton AD; LaVan DA; Fahmy TM; Reed MA Label-Free Immunodetection with CMOS-Compatible Semiconducting Nanowires. Nature 2007, 445, 519–522. [PubMed: 17268465]

(54). Elfstrom N; Juhasz R; Sychugov I; Engfeldt T; Karlstrom AE; Linnros J. Surface Charge Sensitivity of Silicon Nanowires: Size Dependence. Nano Lett. 2007, 7, 2608–2612. [PubMed: 17691849]

Author Manuscript Author Manuscript Author Manuscript Author Manuscript

(55). Elfstrom N; Karlstrom AE; Linnros J. Silicon Nanoribbons for Electrical Detection of Biomolecules. Nano Lett. 2008, 8, 945–949. [PubMed: 18266330]

(56). Zhao C; Xu X; Bae SH; Yang Q; Liu W; Belling JN; Cheung KM; Rim YS; Yang Y; Andrews AM; Weiss PS Large-Area, Ultrathin Metal-Oxide Semiconductor Nanoribbon Arrays Fabricated by Chemical Lift-Off Lithography. Nano Lett. 2018, 18, 5590–5595. [PubMed: 30060654]

(57). Zhao C; Xu X; Ferhan AR; Chiang N; Jackman JA; Yang Q; Liu W; Andrews AM; Cho NJ; Weiss PS Scalable Fabrication of Quasi-One-Dimensional Gold Nanoribbons for Plasmonic Sensing. Nano Lett. 2020, 20, 1747–1754. [PubMed: 32027140]

(58). Liao WS; Cheunkar S; Cao HH; Bednar HR; Weiss PS; Andrews AM Subtractive Patterning via Chemical Lift-Off Lithography. Science 2012, 337, 1517–1521. [PubMed: 22997333]

(59). Cao HH; Nakatsuka N; Serino AC; Liao W-S; Cheunkar S; Yang H; Weiss PS; Andrews AM Controlled DNA Patterning by Chemical Lift-Off Lithography: Matrix Matters. ACS Nano 2015, 9, 11439–11454. [PubMed: 26426585]

(60). Andrews AM; Liao WS; Weiss PS Double-Sided Opportunities Using Chemical Lift-Off Lithography. Acc. Chem. Res 2016, 49, 1449–1457. [PubMed: 27064348]

(61). Xu X; Yang Q; Cheung KM; Zhao C; Wattanatorn N; Belling JN; Abendroth JM; Slaughter LS; Mirkin CA; Andrews AM; Weiss PS Polymer-Pen Chemical Lift-Off Lithography. Nano Lett. 2017, 17, 3302–3311. [PubMed: 28409640]

(62). Zhao C; Xu X; Yang Q; Man T; Jonas SJ; Schwartz JJ; Andrews AM; Weiss PS Self-Collapse Lithography. Nano Lett. 2017, 17, 5035–5042. [PubMed: 28737930]

(63). Cao HH; Nakatsuka N; Liao W-S; Serino AC; Cheunkar S; Yang H; Weiss PS; Andrews AM Advancing Biocapture Substrates via Chemical Lift-Off Lithography. Chem. Mater 2017, 29, 6829–6839.

(64). Slaughter LS; Cheung KM; Kaappa S; Cao HH; Yang Q; Young TD; Serino AC; Malola S; Olson JM; Link S; Hakkinen H; Andrews AM; Weiss PS Patterning of Supported Gold Monolayers via Chemical Lift-Off Lithography. Beilstein J. Nanotechnol 2017, 8, 2648–2661. [PubMed: 29259879]

(65). Cao HH; Nakatsuka N; Serino AC; Liao W-S; Cheunkar S; Yang H; Weiss PS; Andrews AM Small-Molecule Patterning via Prefunctionalized Alkanethiols. Chem. Mater 2018, 30, 4017–4030. [PubMed: 30828130]

(66). Cheung KM; Stemer DM; Zhao C; Young TD; Belling JN; Andrews AM; Weiss PS Chemical Lift-Off Lithography of Metal and Semiconductor Surfaces. ACS Mater. Lett 2019, 2, 76–83. [PubMed: 32405626]

(67). Zayats M; Huang Y; Gill R; Ma CA; Willner I. Label-Free and Reagentless Aptamer-Based Sensors for Small Molecules. J. Am. Chem. Soc 2006, 128, 13666–13667. [PubMed: 17044676]

(68). Lee CS; Kim SK; Kim M. Ion-Sensitive Field-Effect Transistor for Biological Sensing. Sensors (Basel) 2009, 9, 7111–7131. [PubMed: 22423205]

(69). Zhang J; Rupakula M; Bellando F; Garcia Cordero E; Longo J; Wildhaber F; Herment G; Guerin H; Ionescu AM Sweat Biomarker Sensor Incorporating Picowatt, Three-Dimensional Extended Metal Gate Ion Sensitive Field Effect Transistors. ACS Sens. 2019, 4, 2039–2047. [PubMed: 31282146]

(70). Keeble L; Moser N; Rodriguez-Manzano J; Georgiou P. ISFET-Based Sensing and Electric Field Actuation of DNA for On-Chip Detection: A Review. IEEE Sens. J 2020, 20, 11044–11065.

(71). Jeon JH; Cho WJ Ultrasensitive Coplanar Dual-Gate ISFETs for Point-Of-Care Biomedical Applications. ACS Omega 2020, 5, 12809–12815. [PubMed: 32548464]

(72). Stern E; Wagner R; Sigworth FJ; Breaker R; Fahmy TM; Reed MA Importance of the Debye Screening Length on Nanowire Field Effect Transistor Sensors. Nano Lett. 2007, 7, 3405–3409. [PubMed: 17914853]

(73). Lee K; Nair PR; Scott A; Alam MA; Janes DB Device Considerations for Development of Conductance-Based Biosensors. J. Appl. Phys 2009, 105, 102046.

(74). Patel BA Continuous Amperometric Detection of Co-Released Serotonin and Melatonin from the Mucosa in the Ileum. Analyst 2008, 133, 516–524. [PubMed: 18365122]

Author Manuscript Author Manuscript Author Manuscript Author Manuscript

(75). Yang H; Thompson AB; McIntosh BJ; Altieri SC; Andrews AM Physiologically Relevant Changes in Serotonin Resolved by Fast Microdialysis. ACS Chem. Neurosci 2013, 4, 790–798. [PubMed: 23614776]

(76). Cheung KM; Abendroth JM; Nakatsuka N; Zhu B; Yang Y; Andrews AM; Weiss PS Detecting DNA and RNA and Differentiating Single-Nucleotide Variations via Field-Effect Transistors. Nano Lett. 2020, 20, 5982–5990. [PubMed: 32706969]

(77). Xiao Y; Qu X; Plaxco KW; Heeger AJ Label-Free Electrochemical Detection of DNA in Blood Serum via Target-Induced Resolution of an Electrode-Bound DNA Pseudoknot. J. Am. Chem. Soc 2007, 129, 11896–11897. [PubMed: 17850085]

(78). Sassolas A; Leca-Bouvier BD; Blum LJ DNA Biosensors and Microarrays. Chem. Rev 2008, 108, 109–139. [PubMed: 18095717]

(79). Chu DKW; Pan Y; Cheng SMS; Hui KPY; Krishnan P; Liu Y; Ng DYM; Wan CKC; Yang P; Wang Q; Peiris M; Poon LLM Molecular Diagnosis of a Novel Coronavirus (2019-nCoV) Causing an Outbreak of Pneumonia. Clin. Chem 2020, 66, 549–555. [PubMed: 32031583]

(80). Fauci AS; Lane HC; Redfield RR Covid-19–Navigating the Uncharted. N. Engl. J. Med 2020, 382, 1268–1269. [PubMed: 32109011]

(81). Behzadirad M; Nami M; Wostbrock N; Zamani Kouhpanji MR; Feezell DF; Brueck SRJ; Busani T. Scalable Top-Down Approach Tailored by Interferometric Lithography to Achieve Large-Area Single-Mode GaN Nanowire Laser Arrays on Sapphire Substrate. ACS Nano 2018, 12, 2373–2380. [PubMed: 29401381]

(82). Cui Y; Wei Q; Park H; Lieber CM Nanowire Nanosensors for Highly Sensitive and Selective Detection of Biological and Chemical Species. Science 2001, 293, 1289–1292. [PubMed: 11509722]

(83). Patolsky F; Zheng G; Lieber CM Fabrication of Silicon Nanowire Devices for Ultrasensitive, Label-Free, Real-Time Detection of Biological and Chemical Species. Nat Protoc 2006, 1, 1711–1724. [PubMed: 17487154]

(84). Hu P; Yan M; Wang X; Han C; He L; Wei X; Niu C; Zhao K; Tian X; Wei Q; Li Z; Mai L. Single-Nanowire Electrochemical Probe Detection for Internally Optimized Mechanism of Porous Graphene in Electrochemical Devices. Nano Lett. 2016, 16, 1523–1529. [PubMed: 26882441]

(85). Knopfmacher O; Tarasov A; Fu W; Wipf M; Niesen B; Calame M; Schonenberger C. Nernst Limit in Dual-Gated Si-Nanowire FET Sensors. Nano Lett. 2010, 10, 2268–2274. [PubMed: 20499926]

(86). Shoorideh K; Chui CO On the Origin of Enhanced Sensitivity in Nanoscale FET-Based Biosensors. Proc. Natl. Acad. Sci. U. S. A 2014, 111, 5111–5116. [PubMed: 24706861]

Author Manuscript Author Manuscript Author Manuscript Author Manuscript

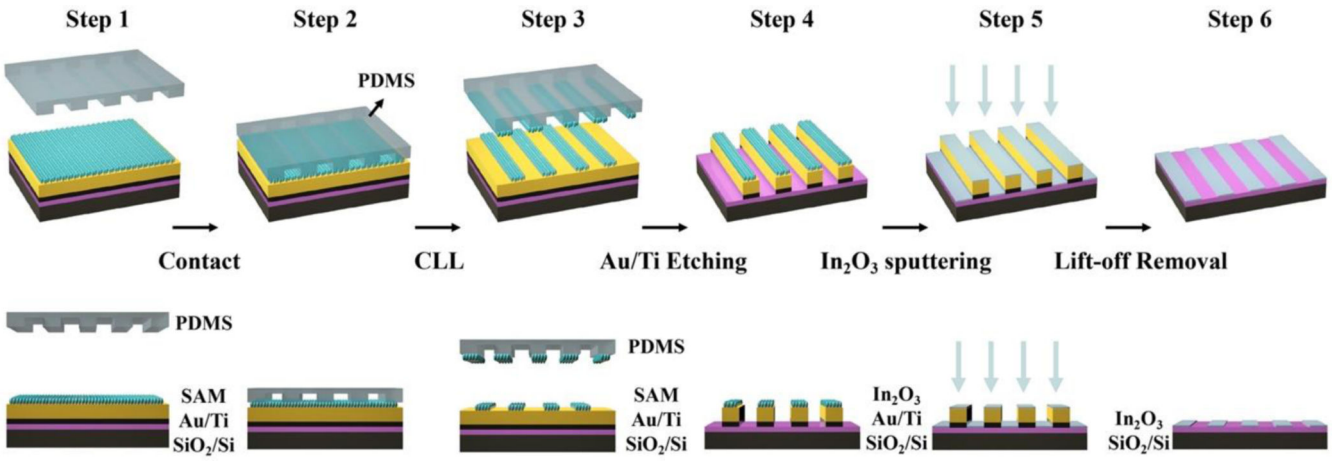

Figure 1.

Schematic illustration of the fabrication process for In_2O_3 nanoribbons. **Step 1**: A Au layer (30 nm) was deposited over Ti (30 nm) on Si/SiO_2 (100 nm). A monolayer of 11-mercapto-1-undecanol was then self-assembled on the Au surface. **Step 2**: An oxygen plasma "activated" polydimethylsiloxane (PDMS) stamp with micro- or nanoribbon features was brought into conformal contact with the substrate. **Step 3**: Stamp removal from the surface, (chemical lift-off lithography, CLL), lifted off self-assembled molecules in the contacted areas. **Step 4**: Selective etching processes removed Au and Ti in the unprotected (contacted) regions on the surface. **Step 5**: Sputtering was used to deposit In_2O_3 (20 nm) over the entire substrate. **Step 6**: The remaining Au/Ti structures were removed to obtain In_2O_3 nanoribbon arrays.

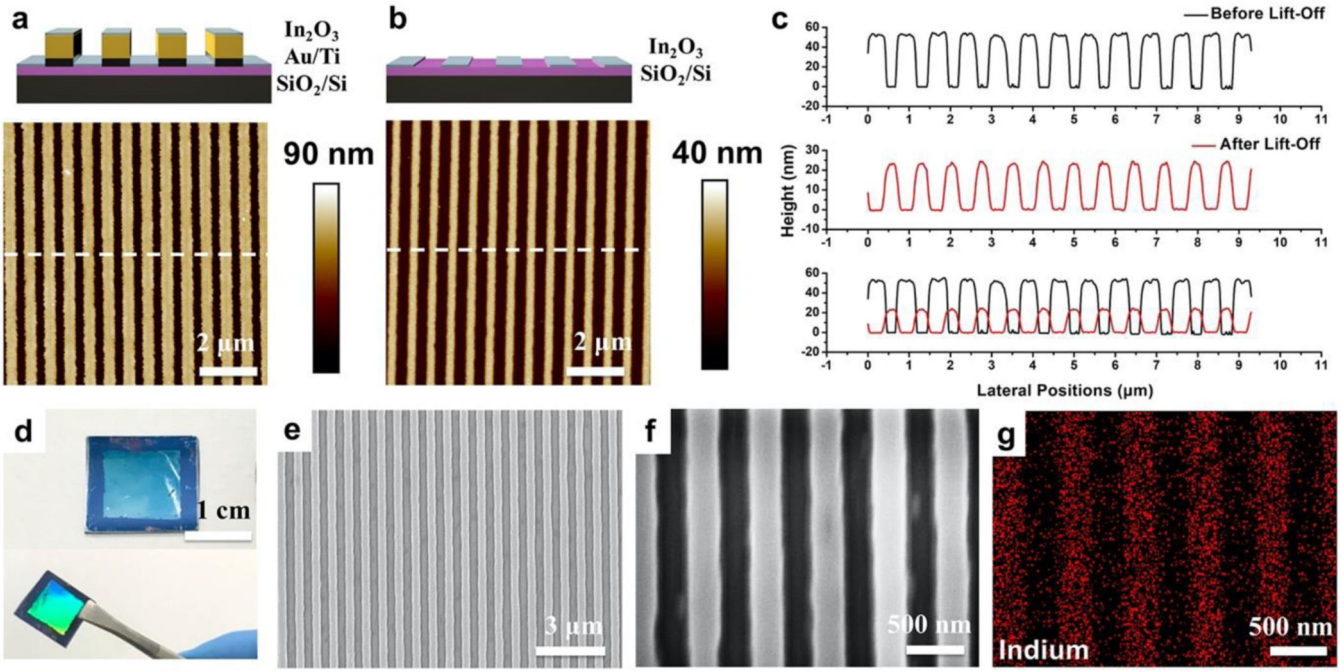

Figure 2.

Atomic force microscope (AFM) images of 350-nm nanoribbon substrates **(a)** before (**Step 5**, Figure 1) and **(b)** after removing underlying Au structures (**Step 6**, Figure 1). **(c)** Height profiles from the AFM images in (a) and (b) across the nanoribbons. **(d)** Photographs of In_2O_3 nanoribbons at different viewing angles. **(e,f)** Scanning electron microscope (SEM) images of 350-nm-wide In_2O_3 nanoribbons. **(g)** Energy-dispersive X-ray mapping of indium corresponding to the SEM image in (f).

Author Manuscript Author Manuscript Author Manuscript Author Manuscript

Author Manuscript Author Manuscript Author Manuscript Author Manuscript

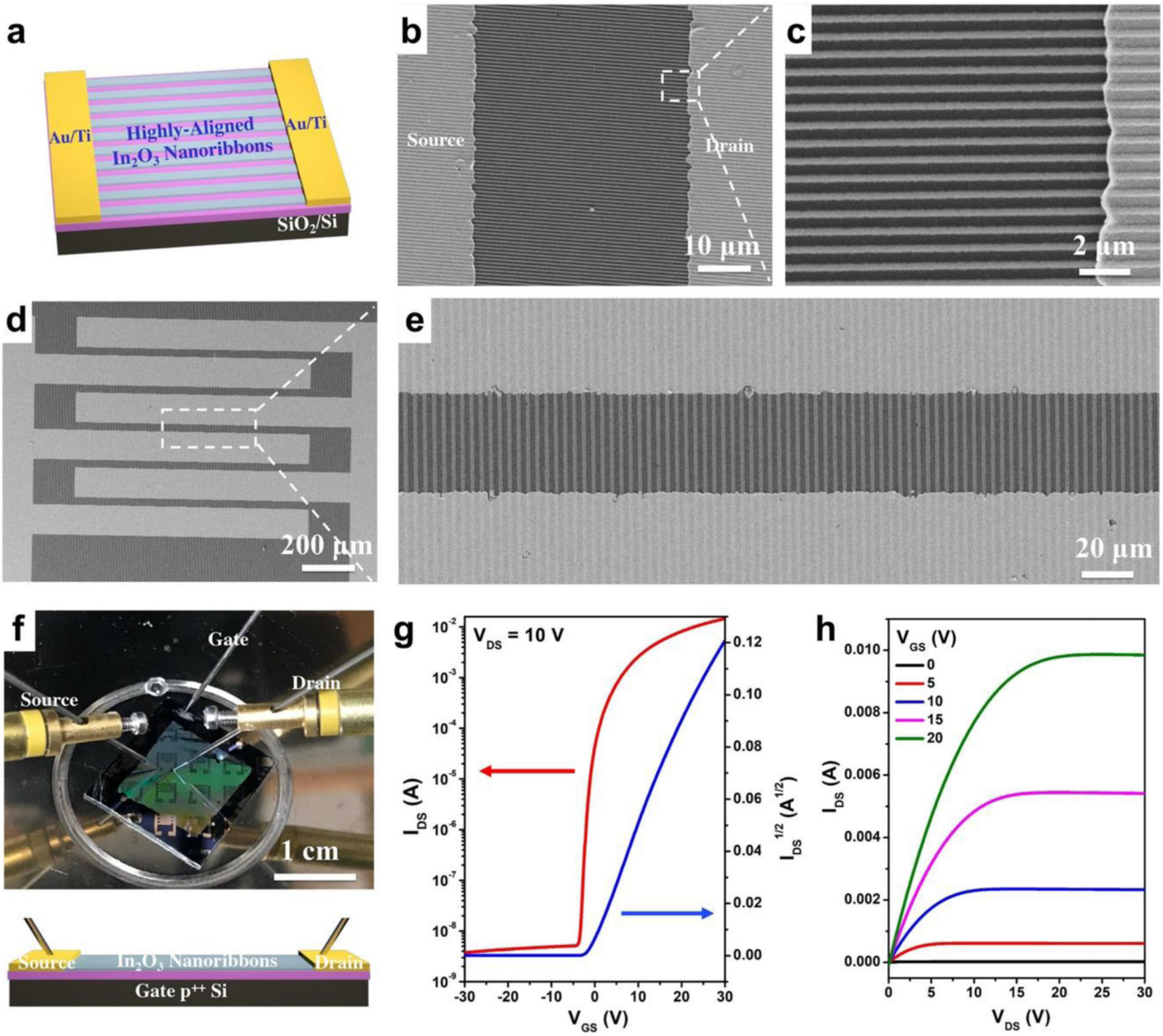

Figure 3. (a)

Schematic illustration of the field-effect transistor (FET) configuration using In_2O_3 nanoribbons (or microribbons) as the channel material aligned perpendicular to source and drain electrodes. **(b,c)** Scanning electron microscope images of 350-nm wide In_2O_3 nanoribbons with source and drain electrodes. **(d,e)** Scanning electron microscope images of 2-μm wide In_2O_3 nanoribbons with source and drain electrodes. **(f)** Photograph (top) and schematic illustration (bottom) of the solid-state measurement set-up for In_2O_3 nanoribbon (and microribbon) FETs, where p^{++} Si serves as the bottom gate. The lavender layer is SiO_2. Transfer **(g)** and output **(h)** characteristics of representative 350-nm In_2O_3 nanoribbon FETs.

Author Manuscript Author Manuscript Author Manuscript Author Manuscript

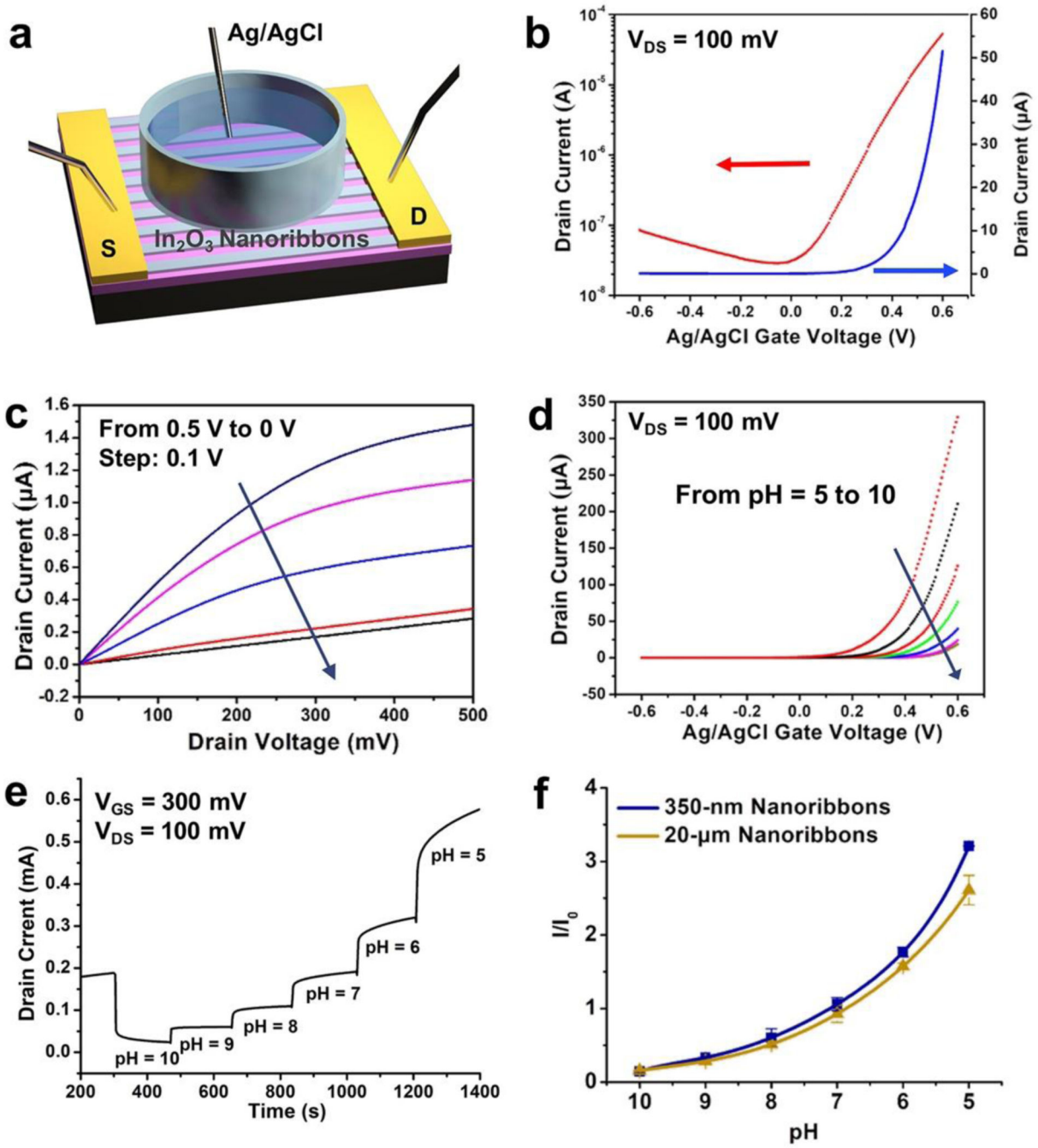

Figure 4. (a)

Schematic illustration of a liquid state measurement where a Ag/AgCl electrode serves as the top-gate. Transfer **(b)** and output **(c)** characteristics of 350-nm-wide In_2O_3 nanoribbon field-effect transistors (FETs) in the liquid-gate setup shown in (a). **(d)** Transfer curves of 350-nm-wide In_2O_3 nanoribbon FETs in solutions of pH 10 to 5. **(e)** Real-time current responses from a representative 350-nm-wide In_2O_3 nanoribbon FET exposed to commercial buffer solutions of pH 10 to 5. **(f)** Current responses relative to baseline for solutions of pH 10 to 5 using 350-nm- or 20-μm-wide ribbon In_2O_3 FETs. I/I_0 is current normalized to the

baseline pH before the experiments (I_0, pH = 7.4). Error bars are standard errors of the means with *N*=3 FETs for each configuration.

Author Manuscript

Author Manuscript

Author Manuscript

Author Manuscript

Author Manuscript Author Manuscript Author Manuscript Author Manuscript

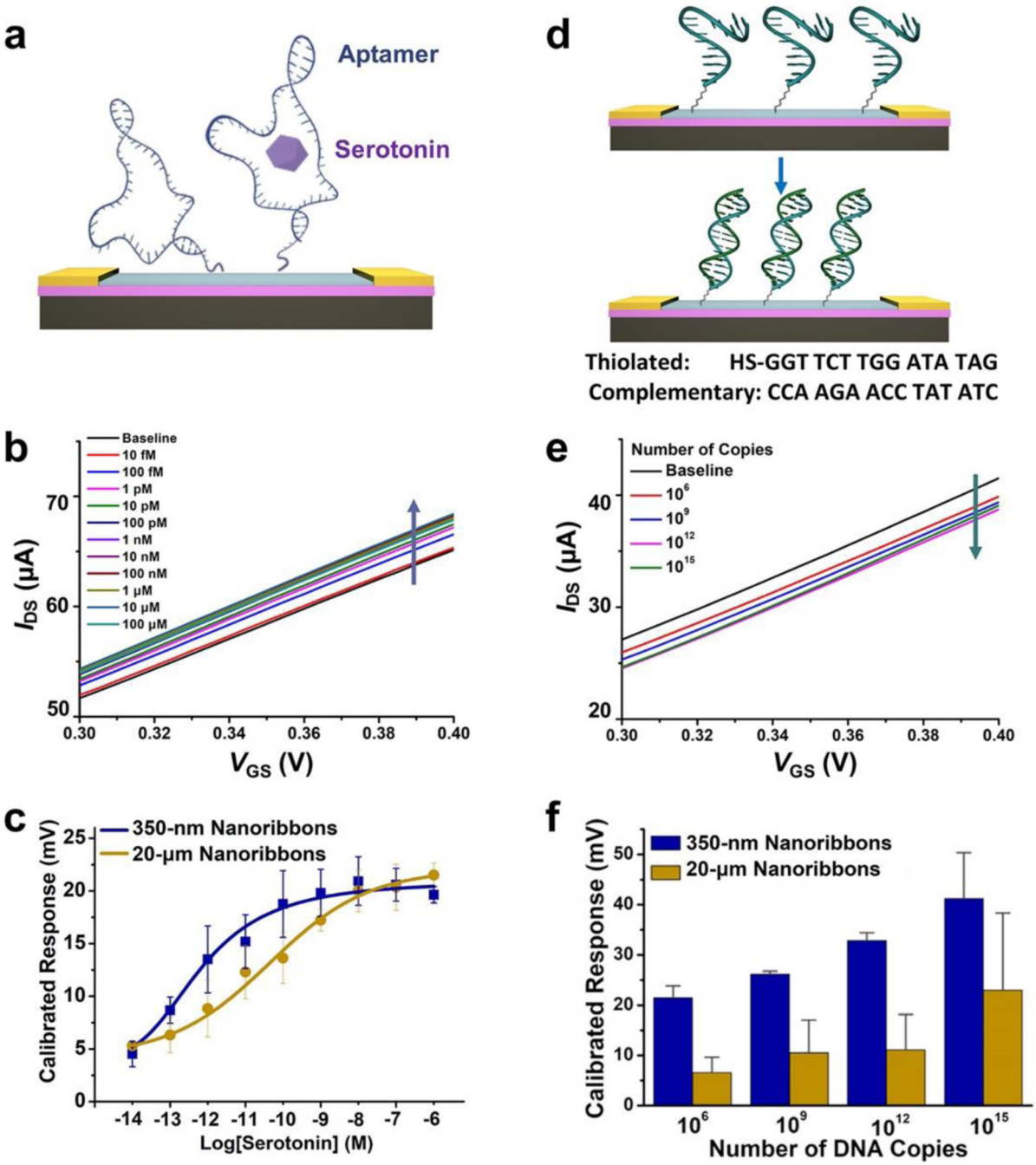

Figure 5. (a)

Schematic illustration of serotonin detection using aptamer-functionalized In_2O_3 field-effect transistor (FET) biosensors. **(b)** Representative transfer curves for serotonin responses from 10 fM to 1 μM for 350-nm In_2O_3 nanoribbon FET biosensors. **(c)** Calibrated response curves for serotonin from 350-nm- *vs* 20-μm-wide In_2O_3 nanoribbon FET biosensors. Error bars are standard errors of the means for N=3 350-nm-wide nanoribbon and N=2 20-μm-wide nanoribbon devices. **(d)** Schematic illustration of DNA hybridization detection. **(e)** Representative transfer curves for responses for complementary DNA hybridization (10^6 to

Author Manuscript Author Manuscript Author Manuscript Author Manuscript

10^{15} copies) for 350-nm In_2O_3 nanoribbon FET biosensors. **(f)** Calibrated responses for complementary DNA hybridization for 350-nm- *vs* 20-μm-wide In_2O_3 nanoribbon FET biosensors. Error bars are standard errors of the means for N=2 350-nm-wide nanoribbon and N=3 20-μm-wide microribbon devices.